Stanford Exploration Project, Report 112, November 11, 2002, pages 65–83

Transformation to dip-dependent Common Image Gathers

Biondo Biondi and William Symes[1]

ABSTRACT

We introduce a new transform of offset-domain Common Image Gathers (CIGs) obtained by wavefield-continuation migration methods. This transformation can be applied to either horizontal-offset CIGs or vertical-offset CIGs. It overcomes the limitations that both kinds of CIGs suffer in the presence of a wide range of reflectors' dips. The result of our transformation is an image cube that is equivalent to the image cube that would have been computed if the offset direction were aligned along the apparent geological dip of each event. The proposed transformation applies a non-uniform dip-dependent stretching of the offset axis and can be efficiently performed in the Fourier domain. Because it is dependent on the image's apparent dip, the offset stretching automatically corrects for the image-point dispersal. Tests on a synthetic data set confirm the potential advantages of the transformation for migration velocity analysis of data containing steeply dipping reflectors.

INTRODUCTION

The analysis of Common Image Gathers (CIG) is an essential tool for updating the velocity model after depth migration. When using wavefield-continuation migration methods, angle-domain CIGs (ADCIGs) are usually used for velocity analysis (Clapp and Biondi, 2000). The computation of ADCIG is based on slant-stack transformation of the wavefield either before imaging (Prucha et al., 1999) or after imaging (Sava et al., 2001; Rickett and Sava, 2001; Biondi and Shan, 2002). In either case, the slant stack transformation is usually applied along the horizontal offset axis.

However, when the geological dips are steep, this "conventional" way of computing CIGs does not produce useful gathers, even if it is kinematically valid for all geological dips that are milder than 90 degrees. As the geological dips increase, the horizontal-offset CIGs (HOCIGs) degenerate, and their focusing around zero offset blurs. This limitation of HOCIGs led both of the authors to independently propose a partial solution to the problem; that is, the computation of CIG along a different offset direction than the horizontal one, and in particular along the vertical direction (Biondi and Shan, 2002). Unfortunately, neither set of angle-domain gathers (HOCIG ad VOCIG) provides useful information for the whole range of geological dips, making their use for velocity updating awkward. While VOCIG are a step in the right direction, they are not readily usable for migration velocity analysis (MVA).

[1]**email:** biondo@sep.stanford.edu

In this paper we present a new method to transform a set of CIGs (HOCIGs and/or VOCIGs) into another set of CIGs. The resulting image cube is equivalent to the image cube that would have been computed by aligning the offset direction along the local geological dips. This transformation applies a non-uniform dip-dependent stretching of the offset axis and can be cheaply performed in the Fourier domain. Because the offset stretching is dependent on the reflector's dip, it also automatically corrects for the image-point dispersal. It thus has the potential to improve substantially the accuracy and resolution of residual moveout analysis of events from dipping reflectors. It has been recognized for long time (Etgen, 1990) that image-point dispersal is a substantial hurdle in using dipping reflections for velocity updating.

The proposed transformation is dependent on the apparent dips in the image cube, and creates an image cube in which the effective offset depends on those apparent dips in an "optimal" way. We will thus refer to the resulting CIGs as dip-dependent offset CIGs (DDOCIGs), and to the transformation as the "transformation to DDOCIGs."

The proposed method is independent from the particular migration method used to obtain the CIGs. The input offset-domain image cube can be computed by either downward-continuation migration (shot profile or survey sinking) or reverse-time migration (Biondi, 2002). The proposed transformation should also improve the accuracy and resolution of velocity analysis applied only to "conventional" HOCIGs. In its most immediate application, it should also improve the image obtained by stacking after a residual moveout correction.

The next section illustrates the problem of HOCIGs and VOCIGs with a real data set from the North Sea that was recorded above a steeply dipping salt edge. The following section introduces the new transformation, that is then tested on a synthetic data set.

COMMON IMAGE GATHERS AND STRUCTURE: A NORTH SEA EXAMPLE

Figures 1–3 illustrate the problem with HOCIGs for a North Sea data set where the salt body has a vertical edge. Because of presence of overturned paths, the data were imaged using a shot-profile reverse time migration.

Figure 1 shows the image extracted at zero offset, which is equivalent to the "stacked image" for Kirchhoff-like migration methods. The vertical edge is well imaged at zero offset, but when we analyze the image as a function of offset at the fixed surface location corresponding to the vertical salt edge (right panel in Figure 2), we immediately notice that, at the depth interval corresponding to the salt edge, there is no focusing along the offset axis. In contrast, the focusing along offset is obvious when we analyze the image at the surface location corresponding to mild reflector dips (left panel in Figure 2). As expected, the lack of focusing in the HOCIGs carries over to the image after transformation to angle domain by slant stacking (Figure 3). In the next section we will explain the degradation of the horizontal-offset CIGs by a simple geometric analysis.

Figure 5 shows a vertical-offset CIG (VOCIG) for the same data set. Since the offset is vertical, the image cube is cut at a constant depth, not at constant surface location. The depth of this CIG corresponds to the black line superimposed onto the image in Figure 4. Now the

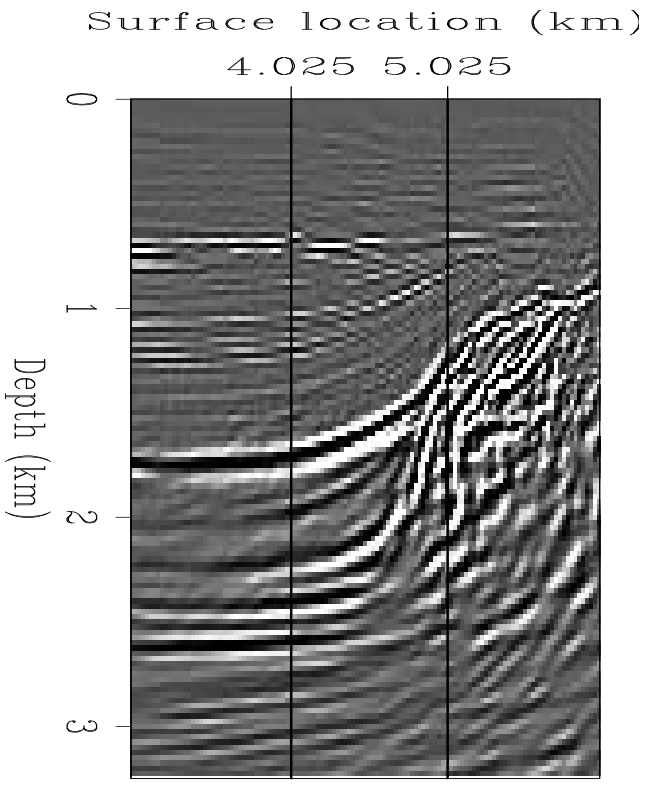

Figure 1: Image of the North Sea data set. The black lines superimposed onto the image indicate the positions of the HOCIGs shown in Figure 2. biondo1-image-cig-new [NR]

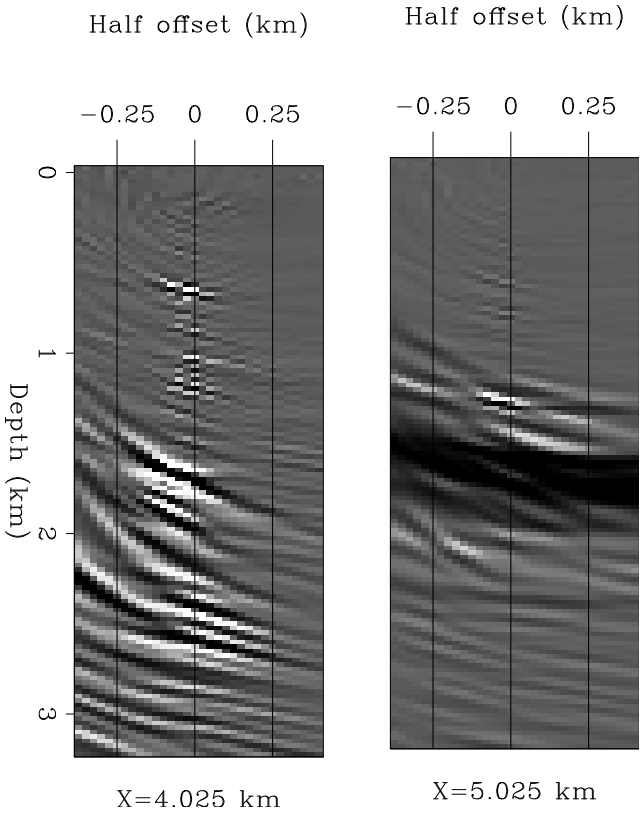

Figure 2: HOCIGs extracted from the prestack image cube. Notice the blurring in the right panel at the depth of the salt edge. biondo1-Cig-all-vz [NR]

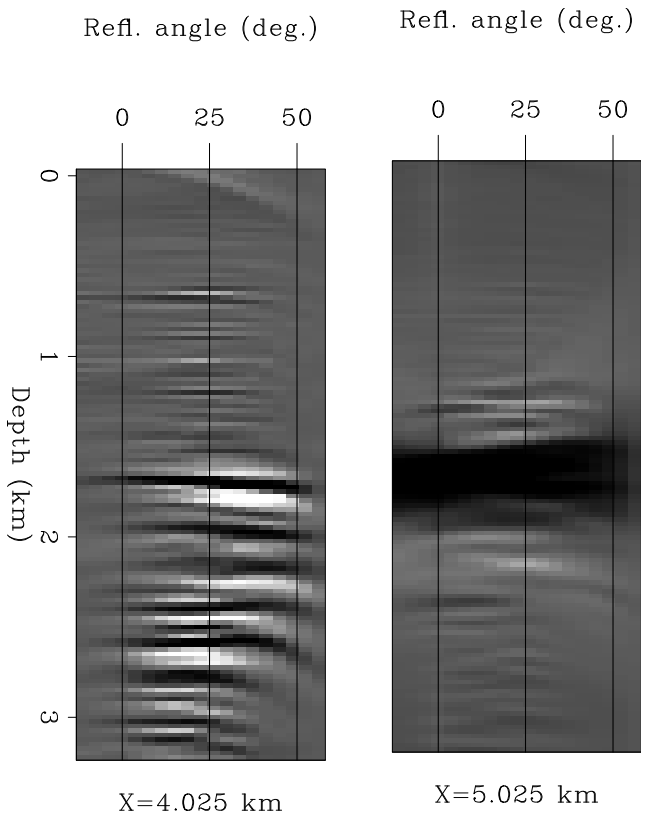

Figure 3: Angle-domain CIGs corresponding to the HOCIGs shown in Figure 2. Notice the blurring in the right panel at the depth of the salt edge. biondo1-Ang-Cig-all-vz [NR]

reflections from the salt edge are focused around zero offset, while the reflections from the flattish reflectors are unfocused. Similarly, after transformation to angle domain (Figure 6) the reflections from the salt edge show a slight moveout that could be used to update the migration velocity function. This task would be impossible if we had to rely solely on the information contained in the ADCIG obtained from HOCIG (Figure 3). However, while the moveouts from the salt edge are clearly interpretable in (Figure 6), the moveouts from flat reflectors are not.

In summary, neither set of CIGs has readily available the information that is needed for velocity updating. In the next section we present a simple method to merge the HOCIG with the VOCIG, and produce a single set of CIGs that satisfies our requirements.

TRANSFORMATION TO DIP-DEPENDENT COMMON IMAGE GATHERS

Two related observations are at the basis of the proposed method. The first one is that the HOCIG and the VOCIG are just particular cases of offset-domain gathers. In general, the offset can be oriented along any arbitrary direction. The second one, is that the offset direction aligned with the apparent geological dip of the imaged event has the unique property of affording the sharpest focusing of the event. The goal of our method is to transform both HOCIGs and VOCIGs into an equivalent set of CIGs (DDOCIGs), for which the effective offset is aligned with the local apparent dips. After the transformation, the DDOCIGs obtained

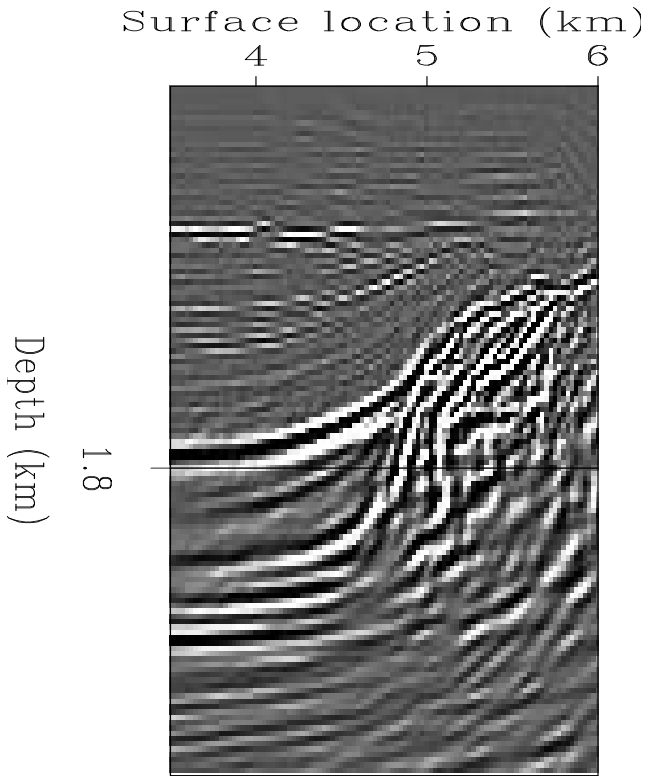

Figure 4: Image of the North Sea data set. The black line superimposed onto the image indicates the depth of the VOCIGs shown in Figure 5 biondo1-image-cig-hz-new [NR]

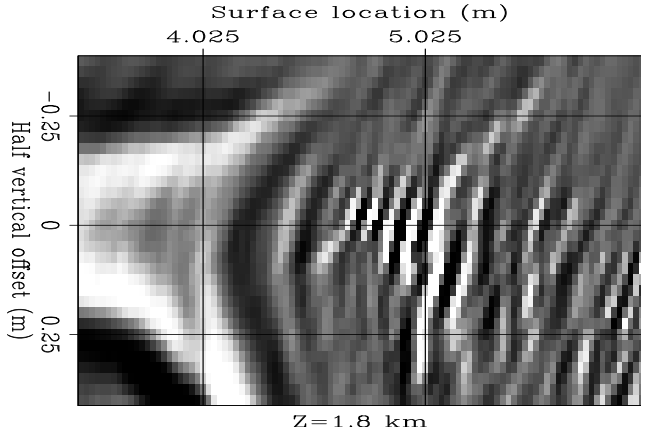

Figure 5: VOCIG extracted from the prestack image cube. Notice the good focus at the horizontal location of the salt edge. biondo1-Cig-1.8-vz-hz [NR]

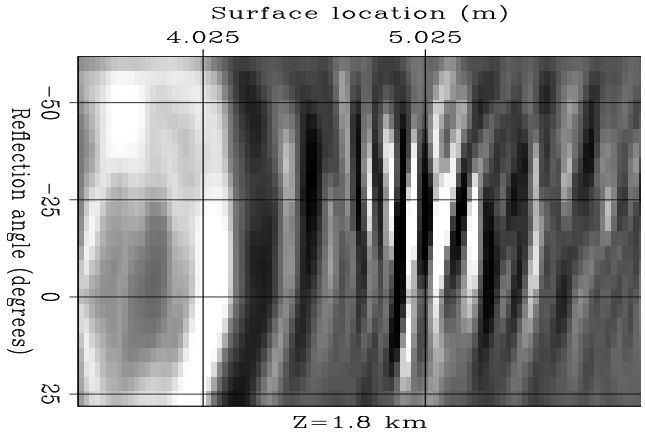

Figure 6: Angle-domain CIG corresponding to the VOCIGs shown in Figure 5. Notice the slight moveout of the the salt edge reflection. biondo1-Ang-Cig-1.8-vz-hz [NR]

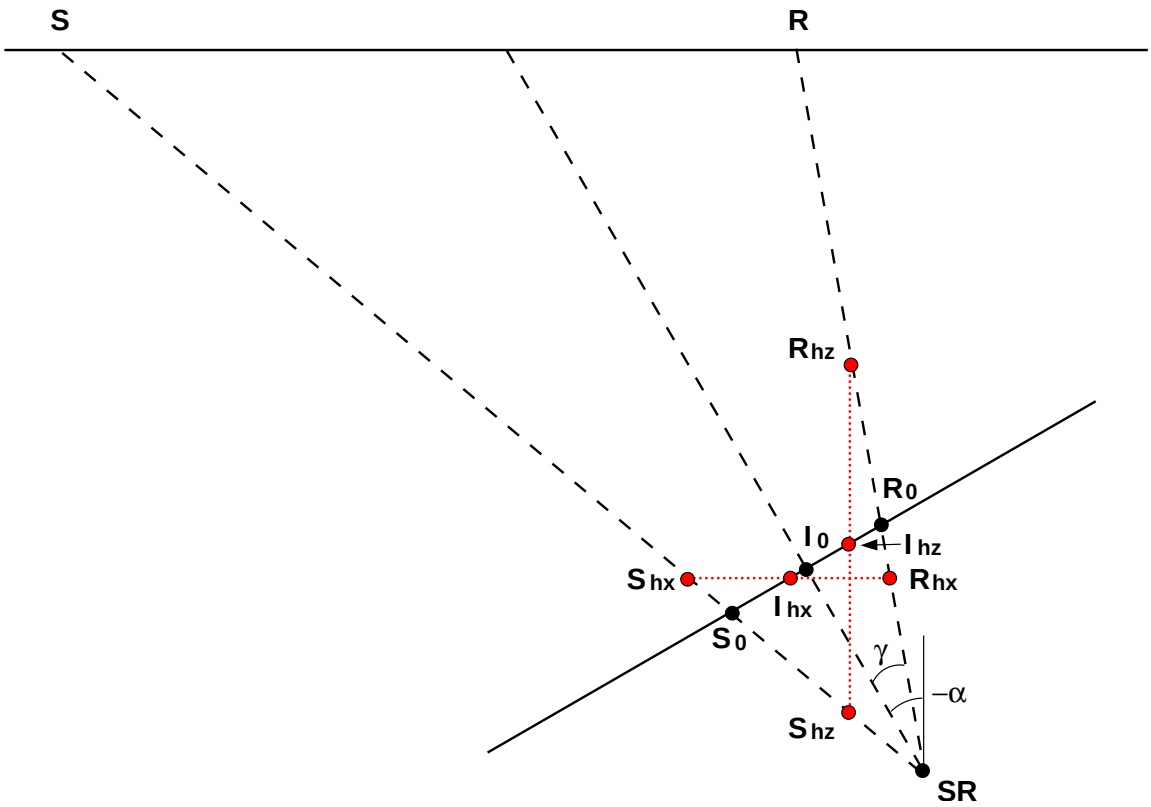

Figure 7: Geometry of the offset-domain CIG for a single event. The migration velocity is assumed to be lower than the true velocity, and thus the events are focused too shallow and above the rays crossing point (SR). biondo1-cig-gen-v4 [NR]

from the HOCIGs and the VOCIGs can be appropriately averaged to obtain a single set of DDOCIGs that contain accurate information for all the geological dips.

Figure 7 illustrates the geometry of the offset-domain CIGs for a single event recorded at the surface for the source location S and receiver location R. The crucial assumption of our geometric construction is that the traveltime along the source ray summed with the traveltime along the receiver ray is the same for all the offset directions and equal to the recording time of the event $\left(|S-S_0|+|R-R_0| = \left|S-S_{x_h}\right|+\left|R-R_{x_h}\right| = \left|S-S_{z_h}\right|+\left|R-R_{z_h}\right|\right)$.

In this sketch, the migration velocity is assumed to be lower than the true velocity, and thus the reflections are imaged too shallow and above the point where the source ray crosses the receiver ray (SR). The line passing through SR, and bisecting the angle formed by the source and receiver ray, is oriented at an angle α with respect to the vertical direction. The angle α is the apparent geological dip of the event after imaging. It would correspond to the true geological dip if the migration velocity were correct. Half of the angle formed between the source and receiver ray is the aperture angle γ.

When HOCIGs are computed, the end point of the source ray (S_{x_h}) and the end point of the receiver ray (R_{x_h}) are at the same depth. The imaging point I_{x_h} is in the middle between

S_{x_h} and R_{x_h} and the imaging offset is $x_h = R_{x_h} - S_{x_h}$. Similarly, when VOCIGs are computed, the end point of the source ray (S_{z_h}) and the end point of the receiver ray (R_{z_h}) are at the same horizontal location. The imaging point I_{z_h} is in the middle between S_{z_h} and R_{z_h} and the imaging offset is $z_h = R_{z_h} - S_{z_h}$. When the offset direction is oriented along the apparent geological dip α (what we called the optimally focusing offset direction), the end point of the source ray is S_0 and the end point of the receiver ray is R_0. The imaging point I_0 is in the middle between S_0 and R_0 and the imaging offset is $h_0 = R_0 - S_0$. It is easy to demonstrate that both I_{x_h} and I_{z_h} lie on the line passing through S_0, I_0 and R_0. The demonstration is based on the assumption that $\left|S_{x_h} - S_0\right| = \left|R_{x_h} - R_0\right|$ and $\left|S_{z_h} - S_0\right| = \left|R_{z_h} - R_0\right|$.

The offsets along the different directions are linked by the following simple relationship, which can be readily derived by trigonometry applied to Figure 7; that is,

$$x_h = \frac{h_0}{\cos\alpha}, \tag{1}$$

$$z_h = \frac{h_0}{\sin\alpha}. \tag{2}$$

Also the shift of the imaging points I_{x_h} and I_{z_h} can be easily expressed in terms of the offset h_0 and the angles α and γ as:

$$\Delta I_{x_h} = \left(I_{x_h} - I_0\right) = -h_0 \tan\gamma \tan\alpha, \tag{3}$$

$$\Delta I_{z_h} = \left(I_{z_h} - I_0\right) = h_0 \frac{\tan\gamma}{\tan\alpha}. \tag{4}$$

Notice the dependence of ΔI_{x_h} and ΔI_{z_h} on the aperture angle γ. This dependence causes events with different aperture angles to be imaged at different locations, even if they originated at the same reflecting point in the subsurface. This phenomenon is related to the well known "reflector-point dispersal" in common midpoint gathers. In this context, this dispersal is a consequence of using a wrong imaging velocity, and we will refer to it as image-point dispersal.

The fact that all three imaging points are aligned along the apparent geological dip allows our transformation to remove the image-point dispersal, and it is crucial to the effectiveness of DDOCIGs. In other words, to transform one set of CIGs into another set we just need to transform the offset axis; the image is then automatically shifted along the apparent geological dip by the right amount. Appendix A demonstrates this fact.

The proposed CIG transformation is a simple dip-dependent non-uniform stretching of the the offset-axis according to the relationships in equations (1) and (2). The transformation is easily implemented in the wavenumber (k_z, k_x) domain, by taking advantage of the well known relationship $\tan\alpha = k_x / k_z$.

After both the HOCIGs and the VOCIGs are transformed, they can be merged together. A simple scheme to merge them is a weighted average, where the weights w_{x_h} and w_{z_h} are set to

$$w_{x_h} = \cos^2\alpha, \tag{5}$$

$$w_{z_h} = \sin^2\alpha. \tag{6}$$

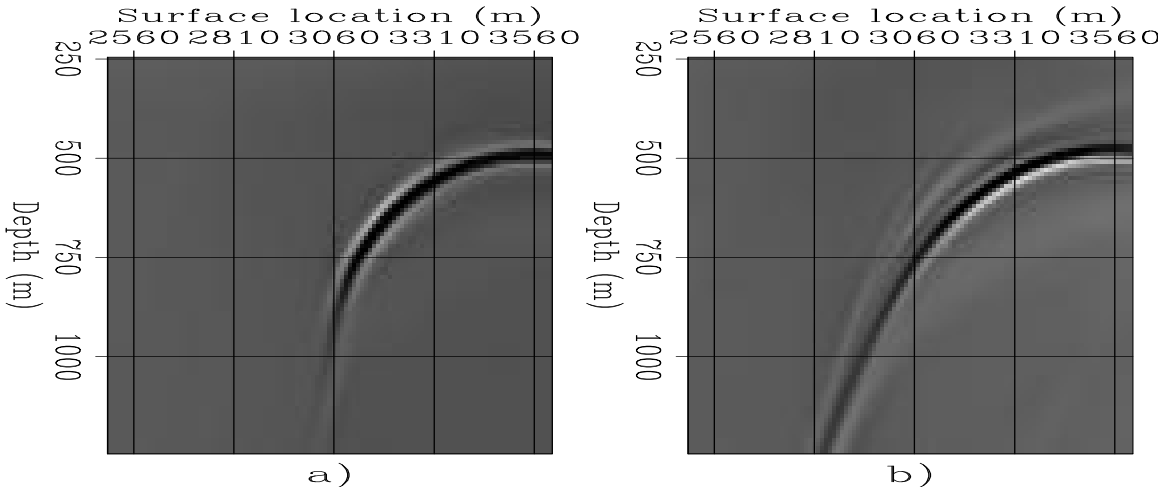

Figure 8: Images of the synthetic data set obtained with a) correct velocity, b) too low velocity by 4%. biondo1-Mig-all-zo-both [CR]

APPLICATION TO A SYNTHETIC DATA SET

To test our proposed method for transforming HOCIGs and VOCIGs into DDOCIGs we modeled and migrated a synthetic data set with a wide range of dips. The reflector has spherical shape with radius of 500 m. The center is at 1,000 meters depth and 3,560 meters horizontal coordinate. The velocity is constant and equal to 2,000 m/s. The data were recorded in 630 shot records. The first shot was located at a surface coordinate of -2,000 meters and the shots were spaced 10 meters apart. The receiver array was configured with asymmetric split-spread geometry. The minimum negative offset was constant and equal to -620 meters. The maximum offset was 4,400 meters for all the shots, with the exception of the first 100 shots (from -2,000 meters to -1,000 meters), where the maximum offset was 5,680 meters in order to record all the useful reflections. To avoid boundary artifacts at the top of the model both sources and receivers were buried 250 meters. Some of the reflections from the top of the sphere were muted out before migration to avoid migration artifacts caused by spurious correlation with the first arrival of the source wavefield.

Figure 8a shows the zero-offset section (stack) of the migrated cubes with the correct velocity (2,000 m/s), and Figure 8b shows the zero-offset section obtained with 4% too low of a velocity (1,920 m/s). Notice that, notwithstanding the large distance between the first shot and the left edge of the sphere (about 5,000 meters), normal incidence reflections illuminate the target only up to about 70 degrees. As we will see in the angle-domain CIGs, the aperture angle coverage shrinks dramatically with the increase of the reflector dip. On the other hand, real data cases are likely to have a vertical velocity gradient that improves the angle coverage of steeply dipping reflectors.

Figures 9 and 10 display sections of the full image cube in the case of the low velocity migration. Figure 9 displays the horizontal-offset image cube, while Figure 10 display the vertical-offset image cube (notice that the offset axis in Figure 10 has been reversed to facil-

itate its visual correlation with the image cube displayed in Figure 9). The side face of the cubes display the CIGs taken at the surface location corresponding to the apparent geological dip of 45 degrees. Notice that the events in the two types of CIGs have comparable shapes, as expected from the geometric analysis presented in the previous section, but their extents are different. The differences between the two image cubes are more apparent when comparing the front faces that show the image at a constant offset of 110 meters (-110 meters in Figure 10). These differences are due to the differences in image-point dispersal for the two offset directions [equation (3) and equation (4)].

Figures 11 and 12 show the image cubes of Figures 9 and 10 after the application of the transformations to DDOCIG, described in equations (1) and (2), respectively. The two transformed cubes are almost identical because both the offset stretching and the image-point dispersal have been removed. The only significant differences are visible in the front face for the reflections corresponding to the top of the sphere. These reflections cannot be fully captured within the vertical-offset image cube because the expression in equation (2) diverges as α goes to zero. Similarly, reflections from steeply dipping events are missing from the horizontal-offset image cube because the expression in equation (1) diverges as α goes to 90 degrees.

The previous figures demonstrate that the proposed transformation converts both HOCIGs and VOCIGs into equivalent DDOCIGs that can be constructively averaged to create a single set of DDOCIGs ready to be analyzed for velocity information. In the following figures, we examine the DDOCIGs obtained by averaging the HOCIGs and VOCIGS using the weights in equations (6), and we compare them with the original HOCIGs and VOCIGs.

We start from analyzing the CIGs obtained when the migration velocity was correct. Figure 13 shows the HOCIGs corresponding to different apparent reflector dips: a) 0 degrees, b) 30 degrees, c) 45 degrees, and d) 60 degrees. The quality of the HOCIGs degrades as dip angle increases. Figure 14 shows the VOCIGs corresponding to the same dips as the panels in Figure 13. In this case, the quality of the VOCIGs improves with the reflector dip.

Figure 15 shows the DDOCIGs corresponding to the same dips as the panels in the previous two figures. Notice that the quality of the DDOCIG is similar to the quality of the HOCIG for small dip angles, and it is similar to the quality of the VOCIG for large dip angles. The focusing of the dipping reflectors (e.g. 60 degrees) is worse than the focusing of the flatter reflectors (e.g. 30 degrees) because of incomplete illumination. In general, the quality of the DDOCIG is "optimal," given the limitations posed by reflector illumination.

The next set of three figures (Figure 16–18) shows the previous offset-domain CIGs transformed into angle domain. The effects of incomplete illumination are more easily identifiable in these gathers than the offset-domain gathers. As for the offset-domain gathers, the angle-domain DDCIGs have consistent quality across the dip range, while the angle-domain gathers obtained from both HOCIG and VOCIG degrade at either end of the dip range.

The next six figures display the same kind of gathers as the past six figures, but obtained when the migration velocity was too low by 4%. They are more interesting than the previous ones, since they are more relevant to velocity updating. Notice that the offset range is doubled

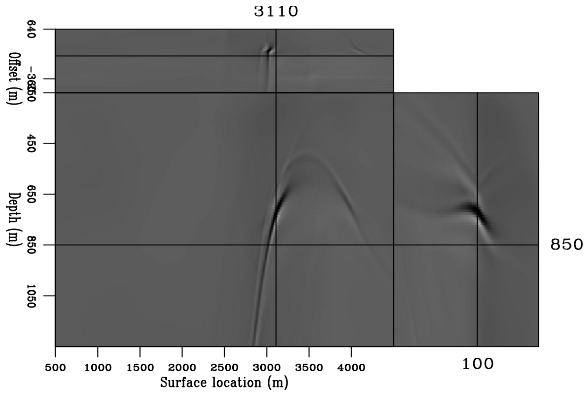

Figure 9: Horizontal-offset image cube when the migration velocity was 4% too low. Notice the differences with the vertical-offset image cube shown in Figure 10. biondo1-Cube-hx-ball-slow-4p [CR]

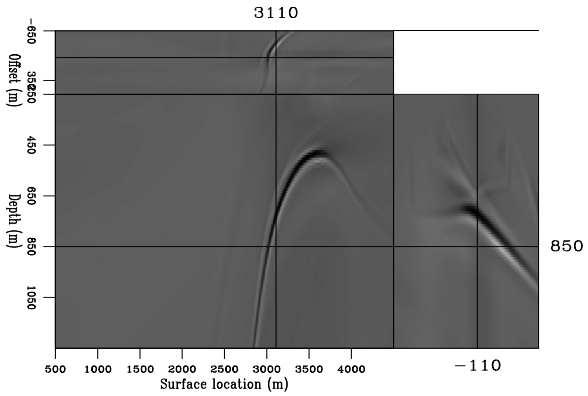

Figure 10: Vertical-offset image cube when the migration velocity was 4% too low. Notice the differences with the horizontal-offset image cube shown in Figure 9. biondo1-Cube-hz-ball-slow-4p [CR]

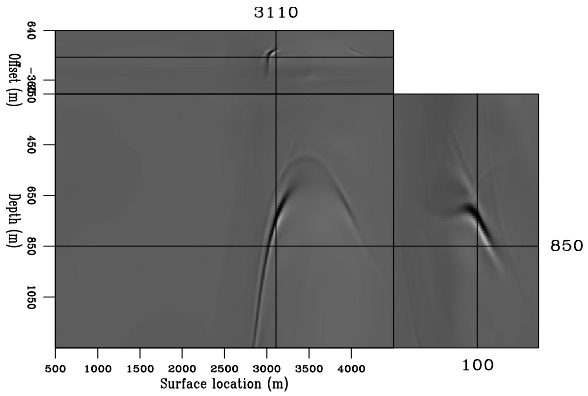

Figure 11: Transformed horizontal-offset image cube. Notice the similarities with the transformed vertical-offset image cube shown in Figure 12. biondo1-Cube-hx-par-ball-slow-4p [CR]

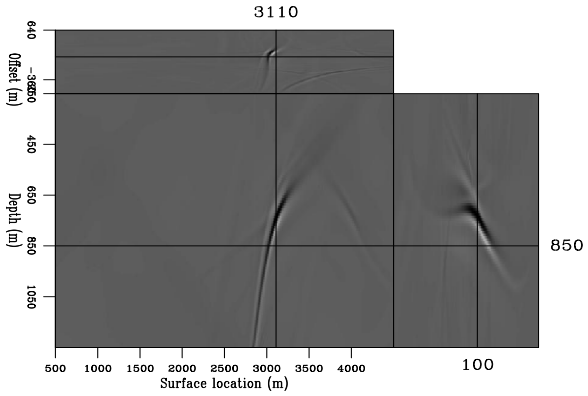

Figure 12: Transformed vertical-offset image cube. Notice the similarities with the transformed horizontal-offset image cube shown in Figure 11. biondo1-Cube-hz-par-ball-slow-4p [CR]

with respect to the previous figures (from $\mp$320 meters to $\mp$640 m) in the attempt to capture within the image cubes all the events, even the ones imaged far from zero offset. For shot profile migration, making the offset range wider is not a trivial additional computational cost.

Figure 19 shows the HOCIGs. The 60 degrees CIG [panel d)] is dominated by artifacts and the corresponding angle-domain CIG shown in Figure 22d would be of difficult use for residual velocity analysis. Figure 20 shows the VOCIGs. As before, the CIGs corresponding to the milder dips are defocused (the artifacts on the left of the panels are caused by the top boundary). The 60 degrees CIG [panel d)] is better behaved than the corresponding HOCIG (Figure 19d), but it is still affected by the incomplete illumination. The DDOCIGs (Figure 21) are the best focused CIGs. Finally the comparison of all the angle-domain CIGs (Figures 22–24) confirm that the DDOCIGS provide the highest resolution and the least-artifact prone ADCIGs, and thus they are the best suited to residual moveout analysis.

CONCLUSIONS

We have introduced a novel transformation of offset-domain Common Image Gathers (CIGs) that applied to either horizontal-offset CIGs (HOCIGs) or vertical-offset CIGs (VOCIGs) transforms them into the equivalent CIGs that would have been computed if the offset direction were aligned along the local geological dip (DDOCIGs). Transformation to DDOCIGs improves the quality of CIGs for steeply dipping reflections by correcting the image cubes from the image-point dispersal. It is particularly useful for velocity analysis when events are not focused around zero offset. The creation of DDOCIGs enables the constructive averaging of HOCIGs with VOCIGs to form DDOCIGs that contain accurate information for all the geological dips. The angle-domain CIGs obtained from the DDOCIGs should provide the best residual moveout information for velocity updating.

We tested the method on a synthetic data set that contains a wide range of dips. The results confirm the theoretical predictions and demonstrate the improvements that are achievable by applying the transformation to DDOCIGs for reflections from steeply dipping reflectors.

ACKNOWLEDGMENTS

We would like to thank Guojian Shan for helping in the computations of the examples of HOCIG and VOCIG from the North Sea data set.

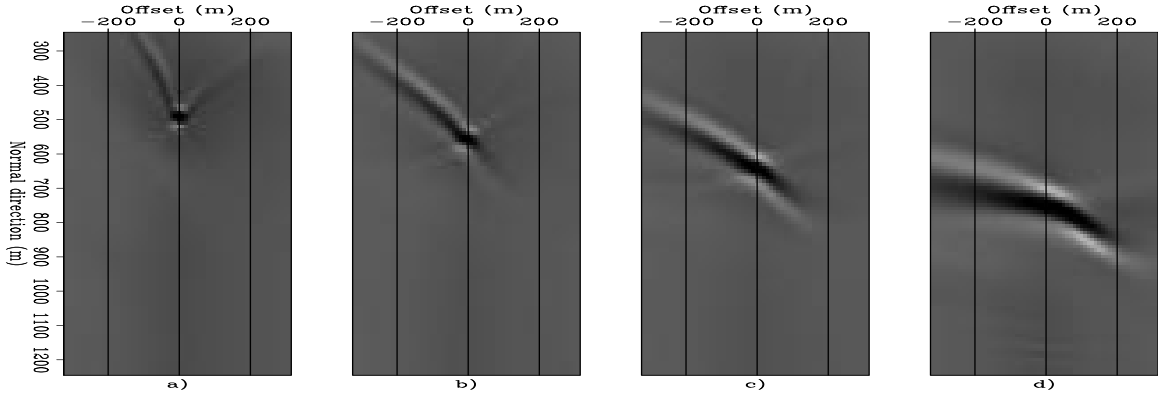

Figure 13: HOCIGs corresponding to different apparent reflector dips: a) 0°, b) 30°, c) 45°, and d) 60°. The migration velocity was correct. biondo1-Cig-hx-ball-allang [CR]

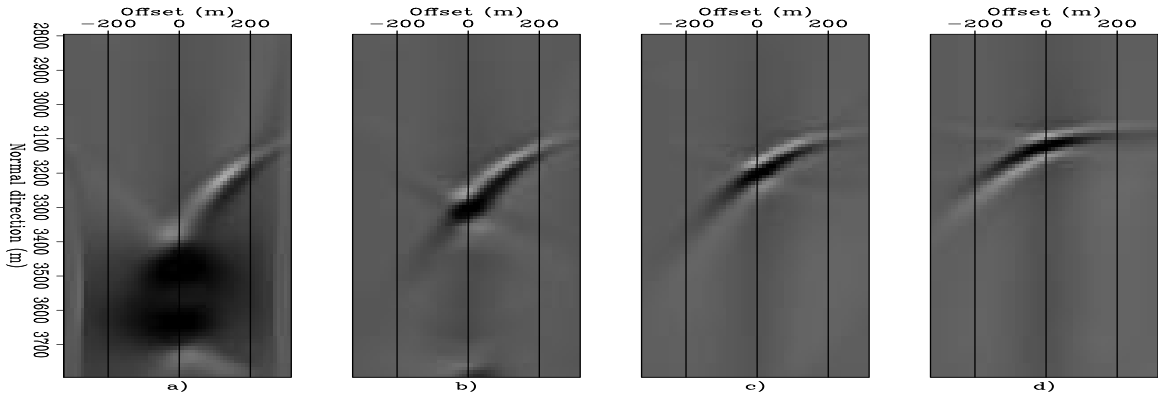

Figure 14: VOCIGs corresponding to different apparent reflector dips: a) 0°, b) 30°, c) 45°, and d) 60°. The migration velocity was correct. biondo1-Cig-hz-ball-allang [CR]

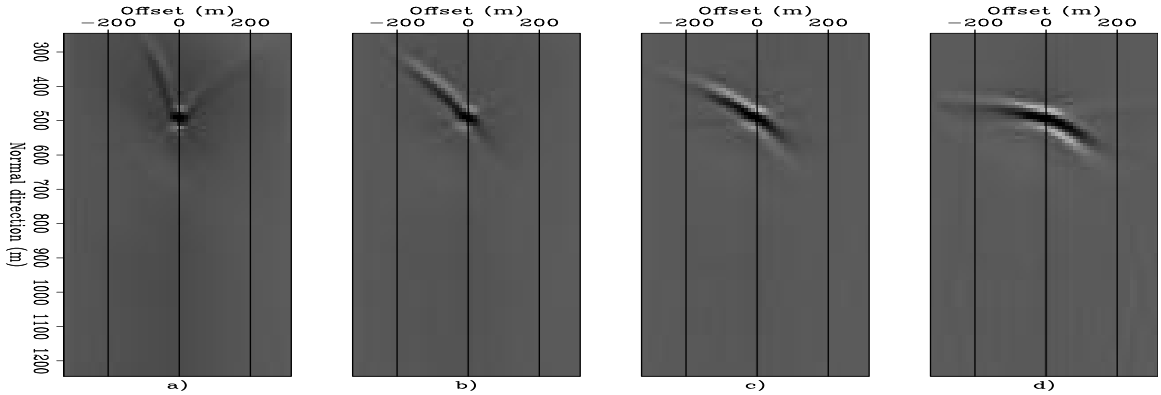

Figure 15: DDOCIGs obtained with the proposed method. The panels correspond to the following apparent reflector dips: a) 0°, b) 30°, c) 45°, and d) 60°. The migration velocity was correct. biondo1-Cig-hrot-ball-allang [CR]

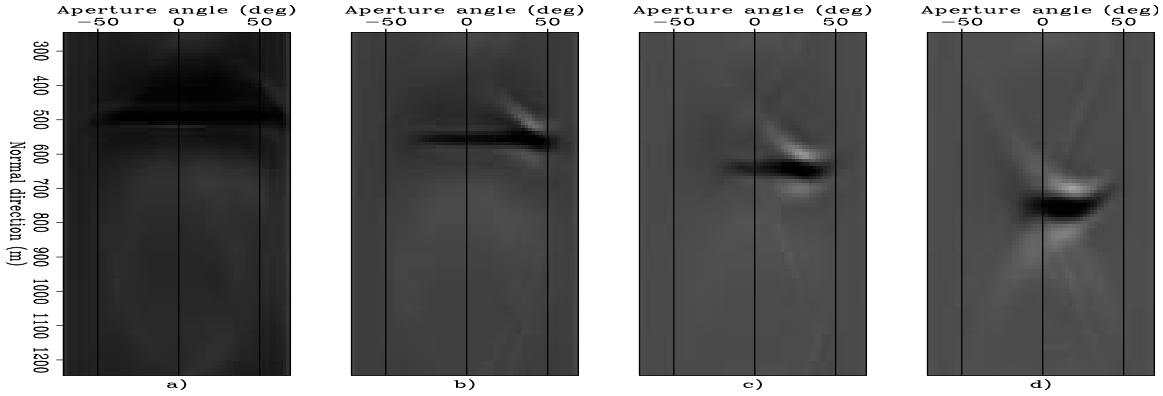

Figure 16: Angle-domain CIGS obtained from the HOCIGs in Figure 13. The panels correspond to the following apparent reflector dips: a) 0°, b) 30°, c) 45°, and d) 60°. The migration velocity was correct. biondo1-Ang-Cig-hx-ball-allang [CR]

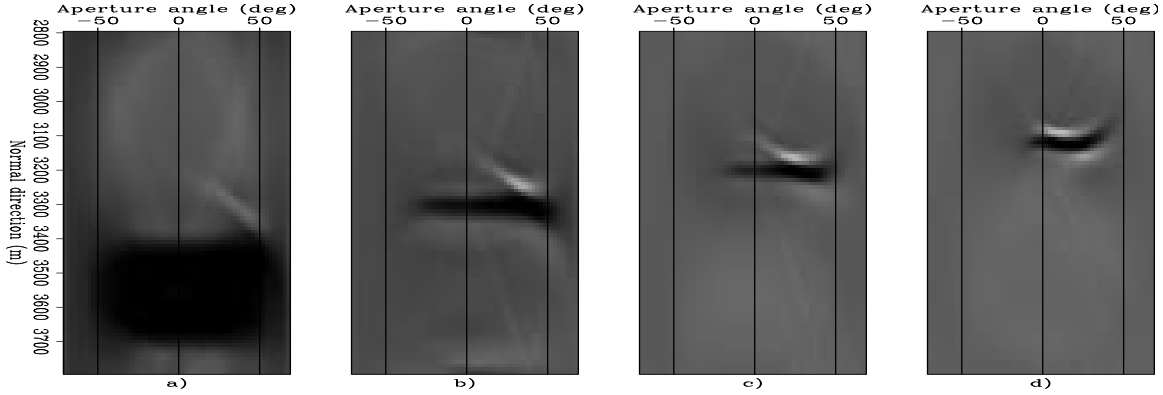

Figure 17: Angle-domain CIGS obtained from the VOCIGs in Figure 14. The panels correspond to the following apparent reflector dips: a) 0°, b) 30°, c) 45°, and d) 60°. The migration velocity was correct. biondo1-Ang-Cig-hz-ball-allang [CR]

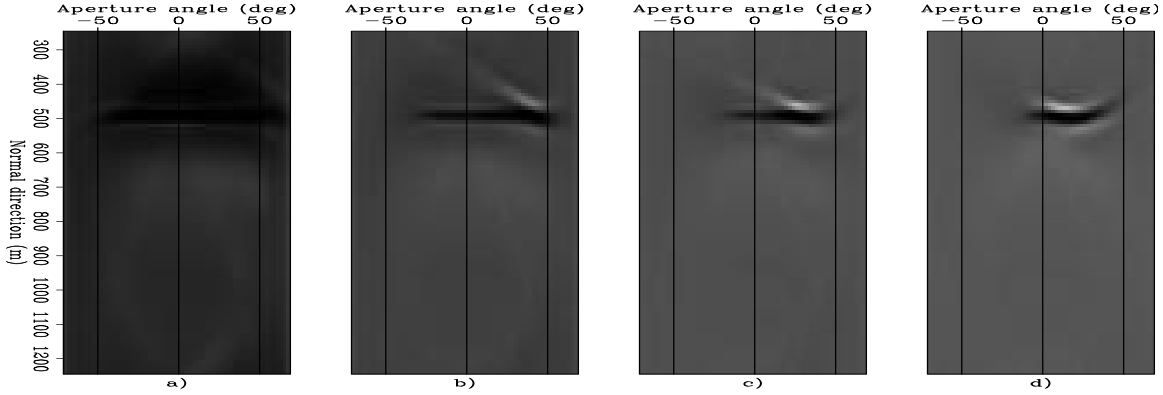

Figure 18: Angle-domain CIGS obtained from the DDOCIGs in Figure 15. The panels correspond to the following apparent reflector dips: a) 0°, b) 30°, c) 45°, and d) 60°. The migration velocity was correct. biondo1-Ang-Cig-hrot-ball-allang [CR]

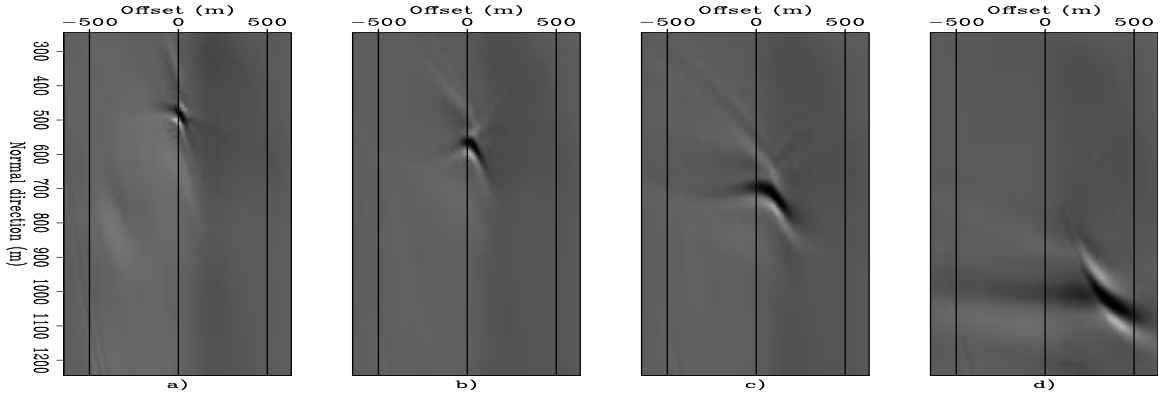

Figure 19: HOCIGs corresponding to different apparent reflector dips: a) 0°, b) 30°, c) 45°, and d) 60°. The migration velocity was 4% too low. biondo1-Cig-hx-ball-allang-slow-4p [CR]

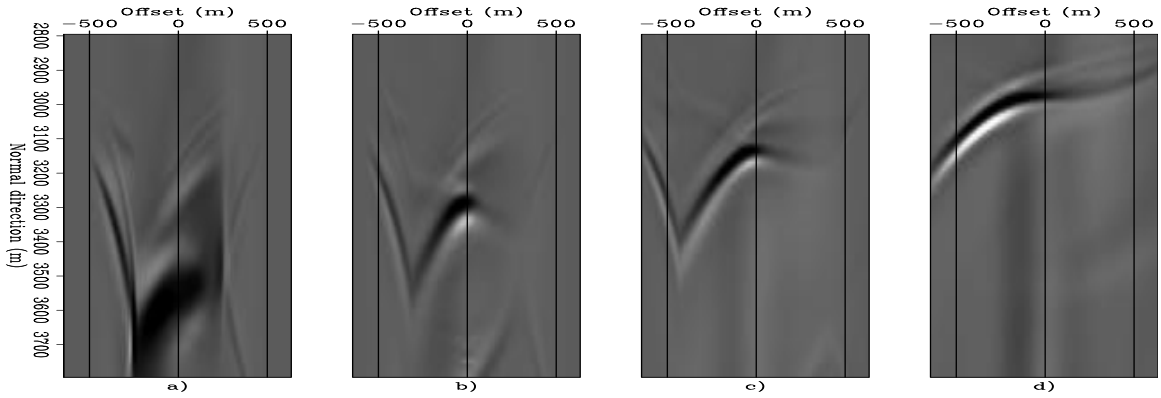

Figure 20: VOCIGs corresponding to different apparent reflector dips: a) 0°, b) 30°, c) 45°, and d) 60°. The migration velocity was 4% too low. biondo1-Cig-hz-ball-allang-slow-4p [CR]

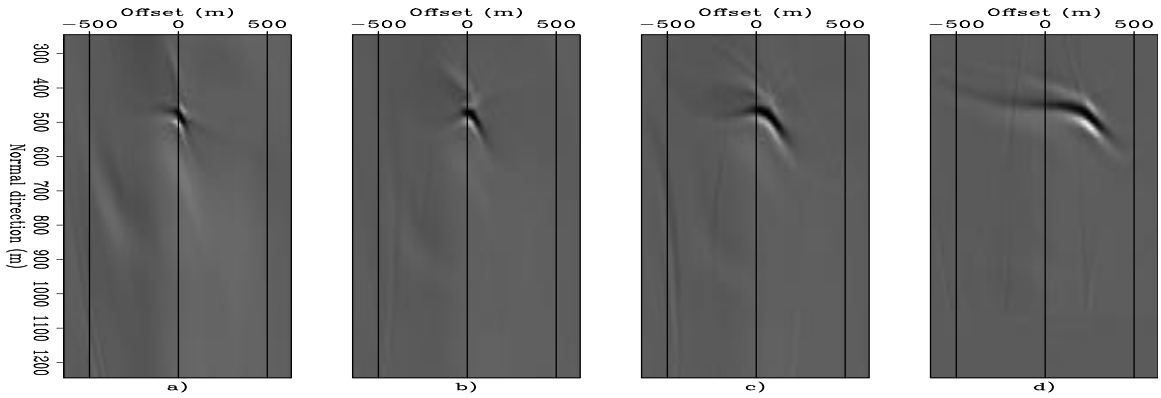

Figure 21: DDOCIGs obtained with the proposed method. The panels correspond to the following apparent reflector dips: a) 0°, b) 30°, c) 45°, and d) 60°. The migration velocity was 4% too low. biondo1-Cig-hrot-ball-allang-slow-4p [CR]

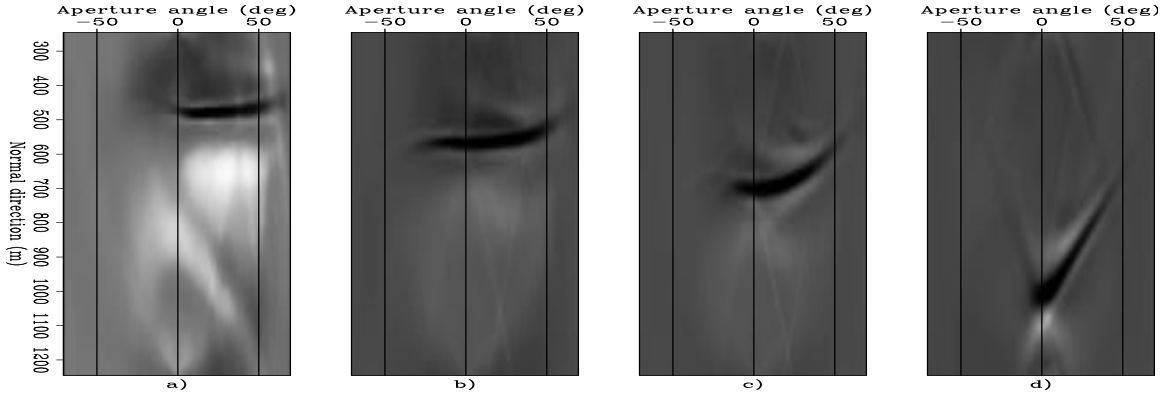

Figure 22: Angle-domain CIGS obtained from the HOCIGs in Figure 13. The panels correspond to the following apparent reflector dips: a) 0°, b) 30°, c) 45°, and d) 60°. The migration velocity was 4% too low. biondo1-Ang-Cig-hx-ball-allang-slow-4p [CR]

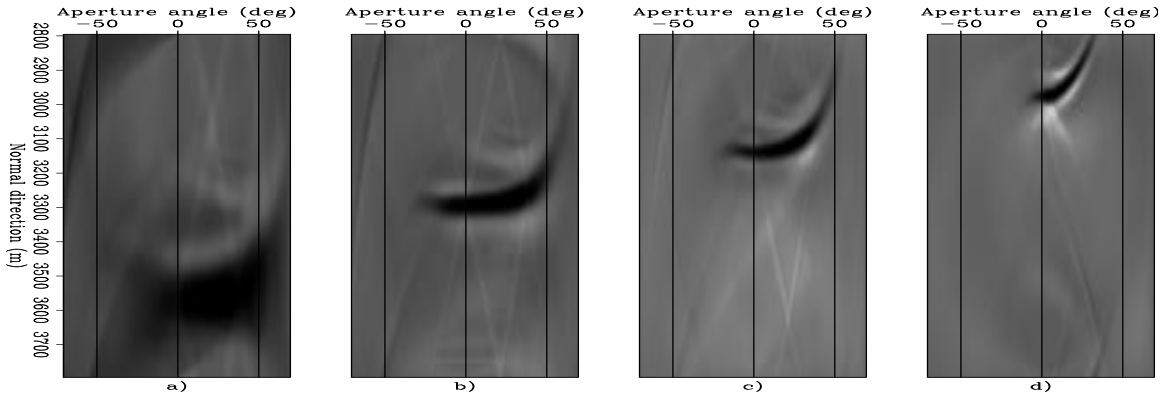

Figure 23: Angle-domain CIGS obtained from the VOCIGs in Figure 14. The panels correspond to the following apparent reflector dips: a) 0°, b) 30°, c) 45°, and d) 60°. The migration velocity was 4% too low. biondo1-Ang-Cig-hz-ball-allang-slow-4p [CR]

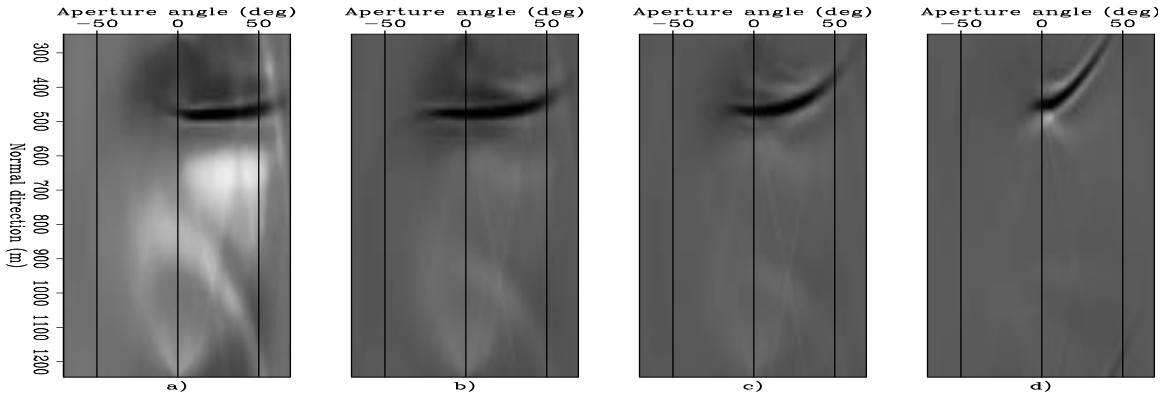

Figure 24: Angle-domain CIGS obtained from the DDOCIGs in Figure 15. The panels correspond to the following apparent reflector dips: a) 0°, b) 30°, c) 45°, and d) 60°. The migration velocity was 4% too low. biondo1-Ang-Cig-hrot-ball-allang-slow-4p [CR]

APPENDIX A

PROOF THAT THE TRANSFORMATION TO DIP-DEPENDENT OFFSET COMMON IMAGE GATHERS (DDOCIG) CORRECTS FOR THE IMAGE-POINT DISPERSAL

This appendix proves that by applying the offset transformations described in equations (1) and (2) we automatically remove the image-point dispersal characterized by equations (3) and (4). The demonstration for the VOCIGs transformation is similar to the one for the HOCIGs transformation, and thus we present only the demonstration for the HOCIGs. HOCIGs are transformed into DDOCIGs by applying the following change of variable of the offset axis x_h, in the vertical wavenumber k_z and horizontal wavenumber k_x domain:

$$x_h = \frac{h_0}{\cos\alpha} = \text{sign}(\tan\alpha) h_0 \sqrt{1+\tan^2\alpha} = \text{sign}\left(\frac{k_x}{k_z}\right) h_0 \left(1+\frac{k_x^2}{k_z^2}\right)^{\frac{1}{2}}. \tag{A-1}$$

For the sake of simplicity, in the rest of the appendix we will drop the sign in front of expression (A-1) and consider only the positive values of k_x/k_z.

We want to prove that applying (A-1) we also automatically shifts the image by

$$\Delta_z I_{x_h} = h_0 \tan\gamma \tan\alpha \sin\alpha \tag{A-2}$$

in the vertical direction, and

$$\Delta_x I_{x_h} = -h_0 \tan\gamma \tan\alpha \cos\alpha \tag{A-3}$$

in the horizontal direction.

The demonstration is carried out into two steps: 1) we compute the kinematics of the impulse response of transformation (A-1) by a stationary-phase approximation of the inverse Fourier transform along k_z and k_x, 2) we evaluate the dips of the impulse response, relate them to the angles α and γ, and then demonstrate that relations (A-3) and (A-2) are satisfied.

Evaluation of the impulse response of the transformation to DDOCIGs

The transformation to DDHOCIG of an image $I_{x_h}(k_z,k_x,x_h)$ is defined as

$$I_0(k_z,k_x,k_h) = \int dh_0 I_0(k_z,k_x,h_0) e^{ik_h h_0} = \int dx_h \left(\frac{dh_0}{dx_h}\right) I_{x_h}(k_z,k_x,x_h) e^{ik_h x_h \left(1+\frac{k_x^2}{k_z^2}\right)^{-\frac{1}{2}}}. \tag{A-4}$$

The transformation to DDHOCIG of an impulse located at $(\bar{z},\bar{x},\bar{x_h})$ is thus (after inverse Fourier transforms):

$$\widetilde{\text{Imp}}(z,x,h_0) = \int dk_h \int dx_h \int dk_x \int dk_z \left(\frac{dh_0}{dx_h}\right) e^{i\left\{k_h\left[\bar{x_h}\left(1+\frac{k_x^2}{k_z^2}\right)^{-\frac{1}{2}}-h_0\right]+k_z(\bar{z}-z)+k_x(\bar{x}-x)\right\}}. \tag{A-5}$$

We now approximate by stationary phase the inner double integral. The phase of this integral is,

$$\Phi \equiv k_h \left[\bar{x_h} \left(1 + \frac{k_x^2}{k_z^2} \right)^{-\frac{1}{2}} - h_0 \right] + k_z (\bar{z} - z) + k_x (\bar{x} - x) \tag{A-6}$$

The stationary path is defined by the solutions of the following system of equations:

$$\frac{\partial \Phi}{\partial k_z} = k_h \bar{x_h} \frac{k_x^2}{k_z^3} \left(1 + \frac{k_x^2}{k_z^2} \right)^{-\frac{3}{2}} + (\bar{z} - z) = 0, \tag{A-7}$$

$$\frac{\partial \Phi}{\partial k_x} = -k_h \bar{x_h} \frac{k_x}{k_z^2} \left(1 + \frac{k_x^2}{k_z^2} \right)^{-\frac{3}{2}} + (\bar{x} - x) = 0, \tag{A-8}$$

By moving both $(\bar{z} - z)$ and $(\bar{x} - x)$ on the right of equations (A-7) and (A-8), and then dividing equation (A-7) by equation (A-8), we obtain the following relationships between $(\bar{z} - z)$ and $(\bar{x} - x)$:

$$\frac{\bar{z} - z}{\bar{x} - x} = -\frac{k_x}{k_z}. \tag{A-9}$$

Furthermore, by multiplying equations (A-7) by k_z and equation (A-8) by k_x, and then substituting them appropriately in the phase function (A-6), we can evaluate the phase function along the stationary path as

$$\Phi_{\text{stat}} = k_h \left[\bar{x_h} \left(1 + \frac{k_x^2}{k_z^2} \right)^{-\frac{1}{2}} - h_0 \right], \tag{A-10}$$

that becomes, by substituting equation (A-9),

$$\Phi_{\text{stat}} = k_h \left\{ -\bar{x_h} \left[1 + \frac{(\bar{z} - z)^2}{(\bar{x} - x)^2} \right]^{-\frac{1}{2}} - h_0 \right\}. \tag{A-11}$$

Notice that the minus sign comes from the sign function in expression (A-1). By substituting expression (A-11) in equation (A-5) it is immediate to evaluate the kinematics of the impulse response as

$$h_0 = -x_h \left[1 + \frac{(\bar{z} - z)^2}{(\bar{x} - x)^2} \right]^{-\frac{1}{2}} \tag{A-12}$$

Evaluation of the image shift as a function of α ad γ

The final step is to take the derivative of the impulse response of equation (A-12) and use the relationships of these derivatives with $\tan\alpha$ and $\tan\gamma$.

$$\frac{\partial z}{\partial x} = \tan\alpha = \sqrt{\frac{x_h^2}{h_0^2} - 1}, \tag{A-13}$$

$$\frac{\partial z}{\partial x_h} = \tan\gamma = (\bar{x}-x)\frac{\frac{x_h}{h_0}}{\sqrt{\frac{x_h^2}{h_0^2}-1}} = (\bar{z}-z)\frac{\frac{x_h}{h_0}}{\frac{x_h^2}{h_0^2}-1}. \tag{A-14}$$

Substituting equations (A-13) and (A-14) into

$$\Delta_z I_{x_h} = \bar{z}-z = h_0 \tan\gamma \tan\alpha \sin\alpha \tag{A-15}$$
$$\Delta_x I_{x_h} = \bar{x}-x = -h_0 \tan\gamma \tan\alpha \cos\alpha. \tag{A-16}$$

.

and after some algebraic manipulations we prove the thesis.

REFERENCES

Biondi, B., and Shan, G., 2002, Prestack imaging of overturned reflections by reverse time migration: 72nd Ann. Internat. Meeting, Soc. of Expl. Geophys., Expanded Abstracts, to be published.

Biondi, B., 2002, Equivalence of source-receiver migration and shot-profile migration: SEP–**112**, 109–116.

Clapp, R., and Biondi, B., 2000, Tau domain migration velocity analysis using angle CRP gathers and geologic constrains: 70th Ann. Internat. Mtg., Soc. Expl. Geophys., 926–929.

Etgen, J., 1990, Residual prestack migration and interval velocity estimation: Ph.D. thesis, Stanford University.

Prucha, M., Biondi, B., and Symes, W., 1999, Angle-domain common-image gathers by wave-equation migration: 69th Ann. Internat. Meeting, Soc. Expl. Geophys., Expanded Abstracts, 824–827.

Rickett, J., and Sava, P., 2001, Offset and angle domain common-image gathers for shot-profile migration: 71th Ann. Internat. Meeting, Soc. Expl. Geophys., Expanded Abstracts, 1115–1118.

Sava, P., Biondi, B., and Fomel, S., 2001, Amplitude-preserved common image gathers by wave-equation migration: 71st Ann. Internat. Meeting, Soc. Expl. Geophys., Expanded Abstracts, 296–299.